Journal of Advanced Ceramics
2023, **12**(5): 930–942
https://doi.org/10.26599/JAC.2023.9220728
ISSN 2226-4108
CN 10-1154/TQ

Research Article

Tunable polarization-drived superior energy storage performance in $PbZrO_3$ thin films

Tiandong Zhang[a,b], Zhuangzhuang Shi[a], Chao Yin[a], Changhai Zhang[a], Yue Zhang[a], Yongquan Zhang[a], Qingguo Chen[a], Qingguo Chi[a,*]

[a]*Key Laboratory of Engineering Dielectrics and Its Application, Ministry of Education, Harbin University of Science and Technology, Harbin 150080, China*
[b]*Department of Materials Science and Engineering, Korea Advanced Institute of Science and Technology, Daejeon 305-701, Republic of Korea*

Received: December 5, 2022; Revised: January 15, 2023; Accepted: January 30, 2023

Abstract: Antiferroelectric $PbZrO_3$ (AFE PZO) films have great potential to be used as the energy storage dielectrics due to the unique electric field (E)-induced phase transition character. However, the phase transition process always accompanies a polarization (P) hysteresis effect that induces the large energy loss (W_{loss}) and lowers the breakdown strength (E_{BDS}), leading to the inferior energy storage density (W_{rec}) as well as low efficiency. In this work, the synergistic strategies by doping smaller ions of Li^+–Al^{3+} to substitute Pb^{2+} and lowering the annealing temperature (T) from 700 to 550 ℃ are proposed to change the microstructures and tune the polarization characters of PZO films, except to dramatically improve the energy storage performances. The prepared $Pb_{(1-x)}(Li_{0.5}Al_{0.5})_xZrO_3$ ($P_{(1-x)}(L_{0.5}A_{0.5})_xZO$) films exhibit ferroelectric (FE)-like rather than AFE character once the doping content of Li^+–Al^{3+} ions reaches 6 mol%, accompanying a significant improvement of W_{rec} of 49.09 J/cm^3, but the energy storage efficiency (η) is only 47.94% due to the long-correlation of FE domains. Accordingly, the low-temperature annealing is carried out to reduce the crystalline degree and the P loss. $P_{0.94}(L_{0.5}A_{0.5})_{0.06}ZO$ films annealed at 550 ℃ deliver a linear-like polarization behavior rather than FE-like behavior annealed at 700 ℃, and the lowered remanent polarization (P_r) as well as improved E_{BDS} (4814 kV/cm) results in the superior W_{rec} of 58.7 J/cm^3 and efficiency of 79.16%, simultaneously possessing excellent frequency and temperature stability and good electric fatigue tolerance.

Keywords: lead zirconate; ionic pair; polarization; breakdown strength; energy storage

1 Introduction

The sustainable developments of the ultra-high-voltage transmission technology, electric vehicles, and electromagnetic weapons have been always accompanied by high-efficiency electric energy storage, and Refs. [1–5] have been committed to improving the energy storage performances of the energy storage devices in recent years. It is well known that commercial energy storage devices mainly include electrochemical

* Corresponding author.
E-mail: qgchi@hrbust.edu.cn

supercapacitors, batteries, and dielectric capacitors [6–9]. Compared with electrochemical supercapacitors and various batteries, dielectric capacitors utilize the electric dipole polarization (P) to store electric energy, which possess extremely fast speed and ultra-high power density (10^8 W/kg) in response to the electric field (E) [10]. Besides, as the whole solid-state device, dielectric capacitors also have significant advantages over electrochemical capacitors in terms of electrical cycle life, thermal stability, and ease of manufacture. Consequently, dielectric capacitors have played an irreplaceable role in pulse discharge systems and power conditioning devices, such as hybrid electric vehicles and electromagnetic catapults [11,12].

Antiferroelectric (AFE) materials represented by $PbZrO_3$ (PZO) have been extensively studied in the field of the dielectric energy storage due to their unique E-induced phase transitions and near-zero remanent polarization (P_r) [10–14]. However, the serious polarization hysteresis during the AFE/ferroelectric (FE) phase transformation process always accompanies an amount of energy loss (W_{loss}) and low energy storage efficiency (η), as well as inferior electric-field tolerance comparing to those of FE ones, resulting in a low energy storage density (W_{rec}).

W_{rec} and η are two critical parameters for evaluating the energy storage performances of capacitor dielectrics. As shown in Fig. S1 in the Electronic Supplementary Material (ESM), W_{rec} and η can be represented by the integrated area in the hysteresis loops (P–E loops) and calculated according to Eqs. (1) and (2), respectively:

$$W_{rec} = \int_{P_r}^{P_m} E\mathrm{d}P \tag{1}$$

$$\eta = \frac{W_{rec}}{W_{rec} + W_{loss}} \times 100\% \tag{2}$$

where P_m is the maximum P, and P_r is the remanent polarization extracted from P–E loops. According to Eqs. (1) and (2), it is clearly seen that the energy storage performances of PZO-based dielectrics can be optimized by tuning the polariazation behavior of AFE/FE phase transformation, improving the breakdown strength (E_{BDS}) and increasing polarization difference ($P_m - P_r$). Over the past decades, Refs. [13,15–22] on improving the energy storage performances of PZO-based AFE thin films are carried out, such as doping with Ca^{2+}, Ba^{2+}, Sr^{2+}, La^{3+}, Eu^{3+}, and Li^{+}–La^{3+} at the Pb^{2+} site and Ti^{4+}, Sn^{4+}, and Nb^{5+} at the Zr^{4+} site. The previous studies indicate that the crystal lattice strain induced by doping ions has profound influence on the phase structure and E-induced phase transformation; however, the W_{rec} and η values are still not sufficiently improved. Especially, the excessive W_{loss} not only reduces the discharge W_{rec}, but also accelerates the insulation degradation and decreases the operation reliability of dielectric capacitors [15]. Therefore, it is still urgent to find an efficient way to achieve both high W_{rec} and η in PZO-based dielectric films.

It is clear that the polarization process of PZO-based films is closely related to the energy storage performances, and the serious polarization hysteresis and inferior tolerance of E are the key bottlenecks to further improving the energy storage performances. Accordingly, in this work, we propose to effectively tune the polariazation behavior and improve the energy storage performances of PZO thin films by synergistically utilizing smaller ionic pair doping and lowering the annealing temperature (T), as shown in Fig. 1. Specifically, Li^{+}–Al^{3+} ions with small ionic radii are used to substitute Pb^{2+} ions to introduce local lattice stress, as well the low-temperature annealing is employed to control the crystallization degree. The $P_{0.94}(L_{0.5}A_{0.5})_{0.06}ZO$ thin films annealed at 550 ℃ deliver the linear-like polarization behavior rather than the AFE-like or FE-like behaviors annealed at 700 ℃. The low P_r as well as high E_{BDS} leads to the superior W_{rec} of 58.7 J/cm^3 and efficiency of 79.16%, accompanying an excellent frequency and temperature stability and good electric fatigue tolerance.

2 Experimental

2.1 Preparation of $Pb_{(1-x)}(Li_{0.5}Al_{0.5})_xZrO_3$ ($P_{(1-x)}(L_{0.5}A_{0.5})_xZO$) thin films

$P_{(1-x)}(L_{0.5}A_{0.5})_xZO$ thin films were grown on Pt(111)/Ti/SiO_2/Si substrate by chemical solution deposition (CSD). Precursor solution of $P_{(1-x)}(L_{0.5}A_{0.5})_xZO$ (x = 0%, 2%, 4%, 6%, and 8%) was first prepared with lead acetate trihydrate, lithium acetate, and aluminum isopropoxide as solid solutes, zirconium-n-propanol as a liquid solute, and 2-methoxyethanol and acetic acid as solvents. 10% excess of lead acetate was added to the solvent to compensate for the lead loss during the annealing process. Zirconium-n-propanol was added after the mixture cooled down to room temperature,

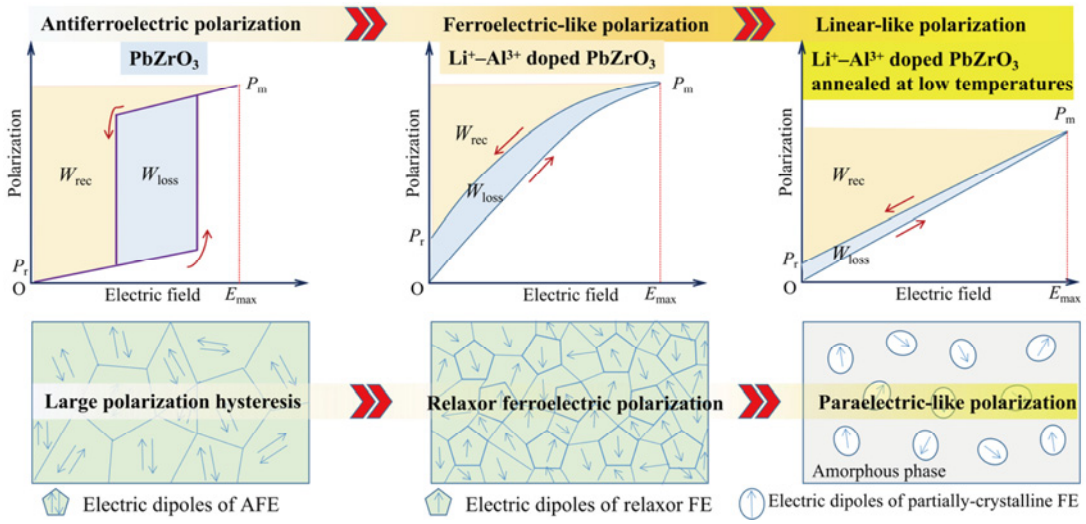

Fig. 1 Schematic diagrams of tunable *P* and energy storage improvement of PZO films by utilizing ionic pair doping and low-temperature annealing.

and the precursor solution concentration was adjusted to 0.3 mol/L by adding 2-methoxyethanol. Then the mixture was stirred at room temperature for 1 h and aged for 24 h. The precursor solution was deposited on the Pt(111)/Ti/SiO_2/Si substrate by the multilayer spin coating procedure for each layer, and the wet film was coated onto the Pt(111)/Ti/SiO_2/Si substrate at 2000 and 4000 r/min for 10 and 20 s, respectively. Each layer of the wet film was pyrolyzed in a plate furnace at 400 ℃ for 3 min to evaporate the organic solvent. The spin coating–pyrolysis procedure was repeated 5 times, and finally the prepared amorphous films were annealed by rapid temperature annealing (RTA; the heating rate is 60 ℃/s) at 700 ℃ for 180 s to obtain the crystalline thin films. Figure S2(a) in the ESM schematically illustrates the fabrication process of $P_{(1-x)}(L_{0.5}A_{0.5})_xZO$ thin films. The $P_{(1-x)}(L_{0.5}A_{0.5})_xZO$ ceramic powders were obtained by conventional temperature annealing (CTA) of the precursor solution annealed at 700 ℃ in the CTA for 1 h. High-purity Pt (99.99%) is sputtered onto the surface of the resultant films to prepare the top electrodes with a size of 4.91×10^{-4} cm^2 by using the direct current (DC) magnetron sputtering under an argon atmosphere, as shown in Fig. S2(b) in the ESM. The digital photograph and cross-sectional scanning electron microscopy (SEM) image of the resultant film are also shown in Figs. S2(c) and S2(d) in the ESM, respectively.

2. 2 Characterization

The phase structures of $P_{(1-x)}(L_{0.5}A_{0.5})_xZO$ thin films and ceramic powders were analyzed by the X-ray diffractometer in the θ–2θ mode at conditions of 40 kV and 40 mA with Cu Kα as the emission source. The cross-sectional structures of $P_{(1-x)}(L_{0.5}A_{0.5})_xZO$ thin films were observed by the SEM (S-4200, HITACHI, Japan). The surface morphologies of the films were observed by the atomic force microscope (AFM; Dimension Icon, Bruker, USA). The *P*–*E* loops of the films were evaluated under different conditions (*E*, temperature, and frequency) using a comprehensive FE performance measuring instrument (Radiant Premier-II, Radiant, USA). The dielectric constant (ε_r) and dielectric loss (tanδ) of the films were measured at a frequency of 0.1 kHz–1 MHz and a temperature range of 20–250 ℃ using a precision impedance analyzer (E4980A, Agilent, USA) with an alternating current (AC) amplitude of 500 mV.

3 Results and discussion

Figure 2(a) shows the X-ray diffraction (XRD) patterns of $P_{(1-x)}(L_{0.5}A_{0.5})_xZO$ thin films with different doping contents of Li^+–Al^{3+} ions (x = 0%, 2%, 4%, 6%, and 8%), and no secondary phases are observed. All the films annealed at 700 ℃ exhibit the preferential (111) orientation induced by the crystal orientation of Pt(111) from the substrate. Figure 2(b) shows that the fine-scan patterns of (111) diffraction peak display a higher 2θ offset with the increase of Li^+–Al^{3+} doping content. Based on the fact that the ionic radii of both Li^+ (~0.076 nm) and Al^{3+} (~0.0535 nm) are much less than

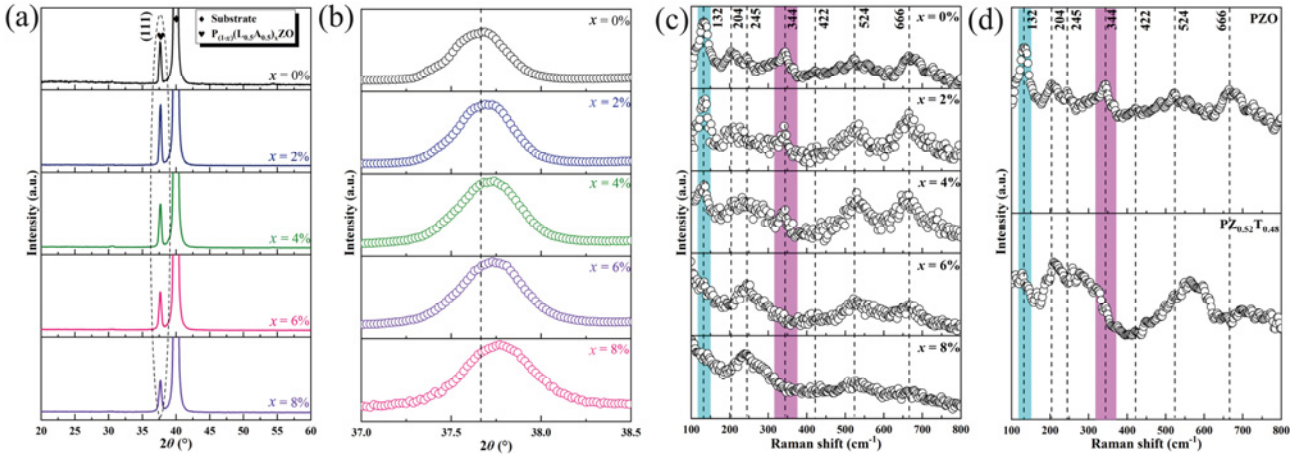

Fig. 2 (a) XRD patterns and (b) fine-scan (111) diffraction peaks for $P_{(1-x)}(L_{0.5}A_{0.5})_xZO$ films. Raman spectra of (c) $P_{(1-x)}(L_{0.5}A_{0.5})_xZO$ thin films and (d) AFE PZO and FE $PZ_{0.52}T_{0.48}$ films.

that of Pb^{2+} (~0.119 nm), the interplanar spacing gradually decreases with the increase of the Li^+–Al^{3+} ion content. The offset of (111) diffraction peak also indicates the successful substitution of Li^+ and Al^{3+} with Pb^{2+} site in the PZO crystal lattices. In addition, the SEM images show the $P_{(1-x)}(L_{0.5}A_{0.5})_xZO$ films' compact microstructure, and the total thickness is about 300 nm, as shown in Fig. S3 in the ESM.

In order to illustrate the changes in the phase structure after doping Li^+–Al^{3+} ions, the Raman scattering spectra are measured from 100 to 800 cm^{-1}, as shown in Fig. 2(c), where the spectrum for the typical FE $PbZr_{0.52}Ti_{0.48}O_3$ ($PZ_{0.52}T_{0.48}$) thin film is used for comparison, as shown in Fig. 2(d). For pure PZO films, the bands in the low-frequency region below 150 cm^{-1} can be assigned to the Pb–ZrO_3 lattice modes, and the bands of 204 and 245, 344 and 422, and 524 and 666 cm^{-1} correspond to the bending mode of Zr–O–Zr, the torsion mode of ZrO_3, and the vibrational mode of Zr–O stretching motion, respectively [23–25]. Obviously, both of the peaks at 132 and 344 cm^{-1} are disappeared when the doping content of Li^+–Al^{3+} ions reaches 6%, which is mostly similar to that of FE $PZ_{0.52}T_{0.48}$, indicating the occurrence of AFE-relaxor FE phase transition at room temperature due to doping smaller ions. It has been reported that the Raman peak at 132 cm^{-1} gradually softens with the increasing temperature and disappears around 234 ℃ (Curie temperature (T_C)), attributing to the phase transition from AFE orthorhombic phase to relaxor FE rhombohedral or paraelectric (PE) cubic phase with the increasing temperature [26]. According to the Raman spectra results, one can deduce that doping Li^+–Al^{3+} ions could improve the FE phase stability instead of the AFE phase stability. This phenomenon is significantly different from that reported in Refs. [21,25,27,28] that doped with smaller ions at the Pb^{2+} site to improve the AFE phase stability of PZO films, instead, which is similar to that doped with smaller ions at Zr^{4+} (~0.072 nm) site such as Zr^{4+} substituted by Ti^{4+} (~0.0605 nm) that improves the FE phase stability.

In order to explore the possible mechanism of the enhanced FE phase stability after doping Li^+–Al^{3+} ions, $P_{(1-x)}(L_{0.5}A_{0.5})_xZO$ ceramic powders were prepared to eliminate the substrate-induced stress and individually study the influence of doping ions on the phase stability. The XRD patterns of $P_{(1-x)}(L_{0.5}A_{0.5})_xZO$ ceramic powders are shown in Figs. 3(a) and 3(b). It can be seen that the diffraction peaks of the (200) and (002) crystal planes are located at a lower 2θ and a higher 2θ, respectively, due to the different crystal lattice constants of AFE orthorhombic phase for the undoped PZO. With the increase of Li^+–Al^{3+} doping content, the peak position of the (200) crystal plane moves to a much higher 2θ degree, while the (002) crystal plane is almost unchanged, meaning that Li^+–Al^{3+} ions give priority to distributing along (100) directions instead of random distribution. In Ref. [19], the co-doped ions tend to occupy adjacent Pb^{2+} site to form ionic pair structures in one crystal cell, such as co-doped Li^+–La^{3+} in PZO films. However, compared to the previous studies in Refs. [16,19], doping ions with smaller radii can usually improve the AFE phase stability, such as co-doped Li^+–La^{3+} or single-doped Sr^{2+} in PZO films; conversely, the increased Li^+–Al^{3+} ionic pair doping content enhances the FE phase stability rather than the AFE phase

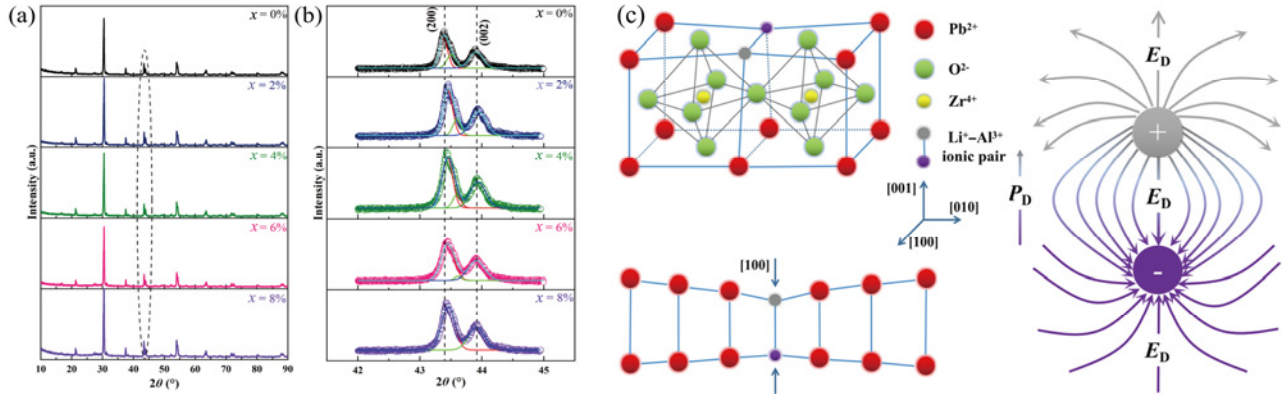

Fig. 3 XRD patterns of (a) $P_{(1-x)}(L_{0.5}A_{0.5})_xZO$ ceramic powders and (b) fine-scan (200) diffraction peak corresponding to (a). (c) Schematic illustrations of the distribution of Li^+–Al^{3+} ionic pair within the same cell and the dipoles induced by Li^+–Al^{3+} ionic pair.

stability. We propose a possible mechanism for this abnormal phenomenon: (1) The Li^+–Al^{3+} ions give priority to forming ionic pairs when the doping content is less than 6%, and the formed ionic pairs act as natural electric dipoles that may promote the adjacent anti-parallel dipoles to be polarized, inducing the AFE to FE phase transformation and improving the FE phase stability. As shown in Fig. 3(c), the electric dipole moment (P_D) generated by the Li^+–Al^{3+} ionic pair creates a local electric field (E_D), which promotes the polarization of the adjacent electric dipoles. (2) We hypothesize that Li^+–Al^{3+} ions are still distributed along the (100)/(010) directions when the doping content is more than 6%, and it may further induce the further increase in 2θ; however, the 2θ of the (002) crystal plane keeps almost unchanged even at x = 8%, indicating that the occupation location of Li^+ or Al^{3+} ions may be changed from Pb^{2+} site to Zr^{4+} to form the anti-defects, resulting in the improvement of FE phase stability [29,30].

The *P*–*E* loops and switching current–*E* loops (*I*–*E* loops) can be used to directly reflect the polarization characters of the modified films, as shown in Figs. 4(a)–4(e); the apparent double *P*–*E* loops and four-peak *I*–*E* loops can be seen for pure PZO films, corresponding to the *E*-induced reversible phase transition from the AFE phase to FE phase. With the increase of Li^+–Al^{3+} doping content, the *E*-induced

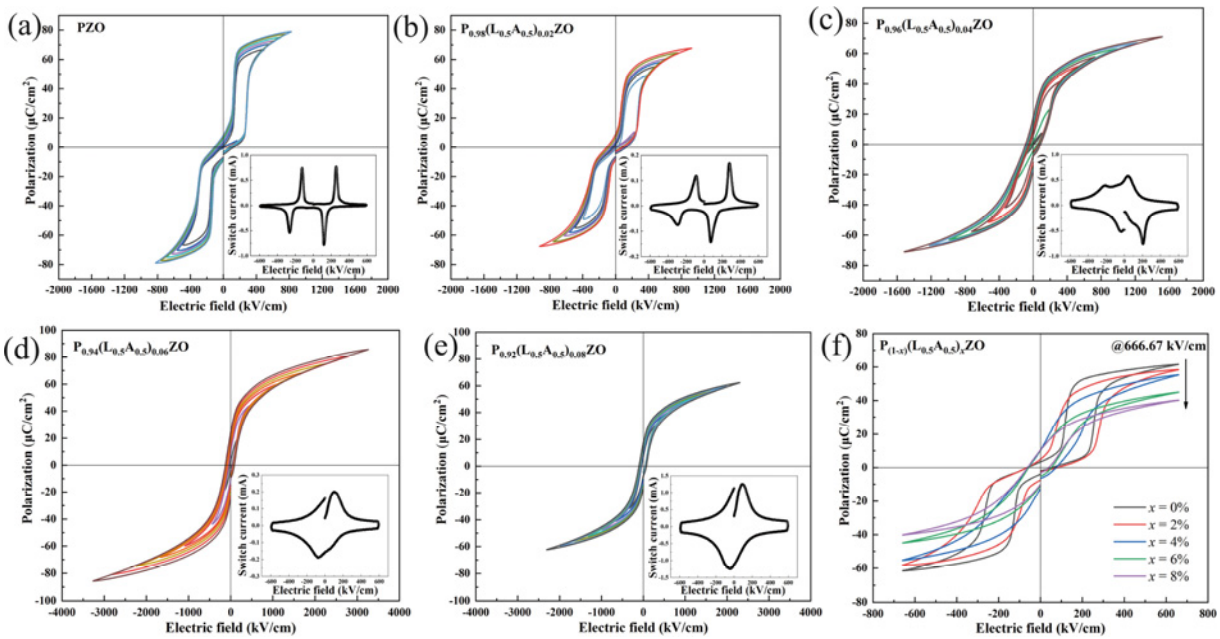

Fig. 4 (a–e) *P*–*E* loops of $P_{(1-x)}(L_{0.5}A_{0.5})_xZO$ thin films. The insets are the corresponding *I*–*E* loops. (f) *P*–*E* loops of the $P_{(1-x)}(L_{0.5}A_{0.5})_xZO$ thin films measured at 666.67 kV/cm.

phase transformation became unobvious, demonstrating the weakened AFE phase stability. When the doping content reaches a critical value of 6%, the double *P*–*E* loops completely disappear and exhibit relaxor FE-like *P*–*E* loops for $P_{0.94}(L_{0.5}A_{0.5})_{0.06}ZO$ and $P_{0.92}(L_{0.5}A_{0.5})_{0.08}ZO$ films. Additionally, *I*–*E* loops show only two-peak instead of four-peak, further proving that the stable phase has completely transformed into the relaxor FE phase when the doping content is more than 6% [31–34]. Furthermore, the P_m value decreases, and the P_r increases with the rising Li^+–Al^{3+} doping content, revealing that the phase structure has been changed by doping Li^+–Al^{3+} ions, as shown in Fig. 4(f).

The temperature dependence of the ε_r and tanδ of $P_{(1-x)}(L_{0.5}A_{0.5})_xZO$ thin films was also investigated. It is well known that the T_C at the maximum value of ε_r corresponds to the phase transition from AFE or FE phase to PE phase. As shown in Fig. 5, it is evident that the ε_r–*T* peak gradually broadens, and the T_C value decreases with the increase of doping content, accompanying by the T_C moving to a higher temperature with the increasing frequency, demonstrating that the AFE/FE–PE phase transition of the $P_{(1-x)}(L_{0.5}A_{0.5})_xZO$ thin films shows the diffusion characteristic with the increase of Li^+–Al^{3+} doping concentration, which is well matched with the variation patterns of the diffusion phase transition caused by doping, as reported in Refs. [35–38]. The diffuseness can be analyzed quantitatively by the modified Curie–Weiss law to access the relaxation degree [39]. Linear fits of the $\ln(1/\varepsilon - 1/\varepsilon_m)$ vs. $\ln(T - T_C)$ of $P_{(1-x)}(L_{0.5}A_{0.5})_xZO$ thin films are shown in the insets of Figs. 5(a)–5(e). The slope of the fitting line (γ) can be used to represent the diffuseness degree, as shown in Fig. 5(f). The γ value for the pure PZO films is 1.02, indicating a first-order phase transition characteristic from AFE to PE [22,38–40]. In comparison, the γ value increases from 1.02 to 1.78 as the Li^+–Al^{3+} ion content increases, demonstrating that Li^+–Al^{3+} ions enhance the diffuseness degree in response to the local lattice stress.

The E_{BDS} value is another important factor to obtain high energy storage properties of thin films and the E_{BDS} value is commonly expressed quantitatively by the two-parameter Weibull distribution function fitting [41,42], as Eqs. (3)–(5):

$$X_i = \ln E_i \tag{3}$$

$$Y_i = \ln(-\ln(1 - P_i)) \tag{4}$$

$$P_i = \frac{i}{n+1} \tag{5}$$

where n is the total number of samples, i is the sample serial number, and E_i is the electrical breakdown strength of the corresponding samples arranged in the ascending order ($E_1 \leqslant E_2 \leqslant \ldots E_i \leqslant \ldots E_n$). P_i is the probability of thin film breakdown. According to

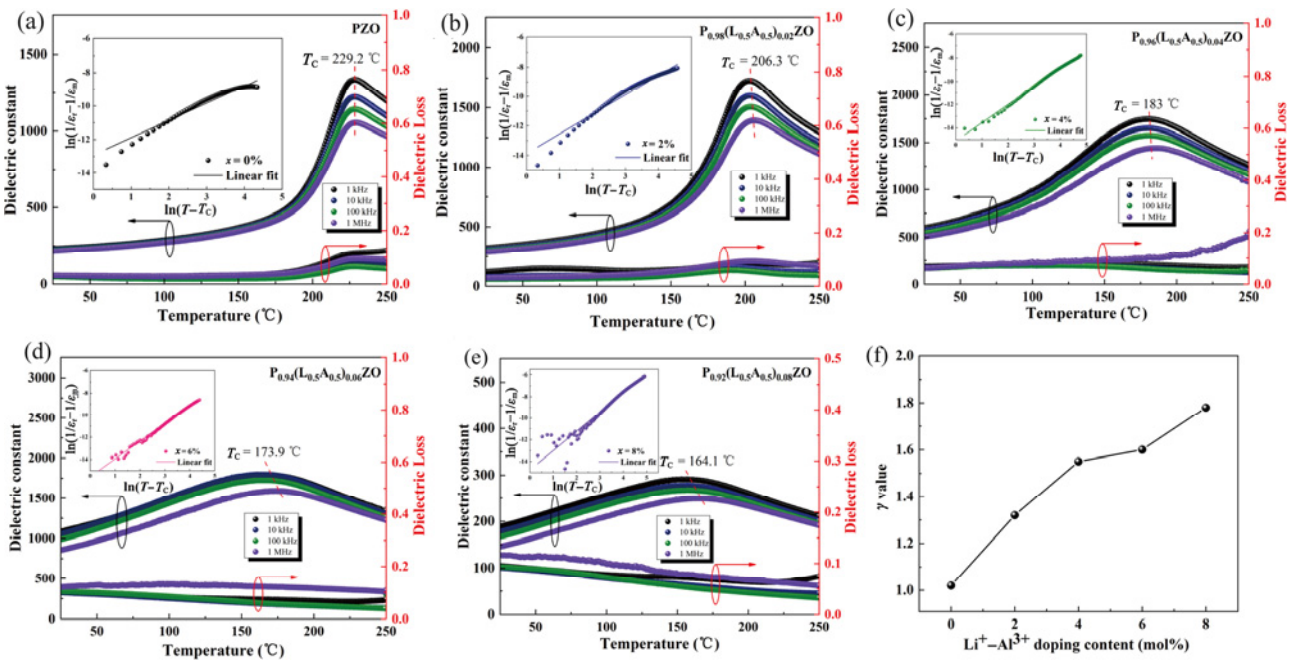

Fig. 5 (a–e) ε_r–*T* and tanδ–*T* curves of $P_{(1-x)}(L_{0.5}A_{0.5})_xZO$ thin films measured from 1 kHz to 1 MHz. The insets show the linear relationships of $\ln(1/\varepsilon_r - 1/\varepsilon_m)$ and $\ln(T - T_C)$. (f) γ values of $P_{(1-x)}(L_{0.5}A_{0.5})_xZO$ thin films.

the two-parameter Weibull distribution function, X_i and Y_i have a linear relationship. The average E_{BDS} value for each sample can be extracted from the intersection point where the fitted line $Y_i(X_i)$ and the horizontal line $Y_i = 0$, the slope of fitted line (β) represents the dispersion of E_{BDS}, reflecting the reliability of E_{BDS} in the thin films. As shown in Figs. 6(a) and 6(b), it can be seen that the E_{BDS} value increases first, and then decreases as the Li^+–Al^{3+} ion content increases. It is well known that the E_{BDS} of AFE is always inferior to that of relaxor FE or normal FE due to the E-induced phase transformation accompanying large electrostriction. With the increase of Li^+–Al^{3+} ion content, the AFE property is gradually weakened, and the E_{BDS} is enhanced accordingly. More importantly, the Li^+–Al^{3+} ionic pairs acting as natural electric dipoles could trap mobile charge carriers and improve the insulation of the films. When the Li^+–Al^{3+} ion content reaches a critical value of 0.06, the largest E_{BDS} of 3888 kV/cm as well as a high β value (36.84) is obtained in $P_{0.94}(L_{0.5}A_{0.5})_{0.06}ZO$ films. However, with the further increase of doping content, the occupation of Li^+–Al^{3+} ions would change from A site into B site, as mentioned in the analyses of Fig. 3(b), which may form cation vacancy, and the destroyed structures of Li^+–Al^{3+} ionic pairs may also lost the ability to restrict mobile charge carriers, leading to the reduction of E_{BDS} in $P_{0.92}(L_{0.5}A_{0.5})_{0.08}ZO$ films. Figure 6(c) shows the P_m, P_r, and $P_m - P_r$ values of $P_{(1-x)}(L_{0.5}A_{0.5})_xZO$ thin films measured at the maximum E (E_{max}) due to the relaxor FE-like characteristics and good electric field endurance, and the maximum values of P_m and P_r are obtained at x = 6%. According to the P–E loops of the $P_{(1-x)}(L_{0.5}A_{0.5})_xZO$ thin films (Fig. 4 and Eqs. (1) and (2)), the W_{rec} and η values of $P_{(1-x)}(L_{0.5}A_{0.5})_xZO$ thin films are obtained, as shown in Fig. 6(d). The maximum W_{rec} values are 10.76, 10.04, 18.63, 49.09, and 21.03 J/cm^3, accompanying η values of 50.93%, 40.07%, 56.19%, 47.94%, and 74.76%, respectively, for $P_{(1-x)}(L_{0.5}A_{0.5})_xZO$ thin films with 0%, 2%, 4%, 6%, and 8% doping contents, respectively. The W_{rec} value of $P_{0.94}(L_{0.5}A_{0.5})_{0.06}ZO$ thin film is improved by 356.2% compared with that of the undoped PZO films. However, it should be noted that although the ultra-high W_{rec} (49.09 J/cm^3) is achieved, a much lower η of 47.94% should be further improved due to that the unreleased stored energy would transfer into Joule heat and threaten the film capacitors' operation efficiency and stability [34–43].

The wide-range frequency response and fatigue endurance are the crucial issues for accessing the operation stability of film capacitors. Figure 6(e) shows the frequency dependence of W_{rec} and η of $P_{0.94}(L_{0.5}A_{0.5})_{0.06}ZO$ thin film at room temperature, and the inset shows the corresponding P–E loops from 50 Hz to 10 kHz measured at 2000 kV/cm. The W_{rec} and η of $P_{0.94}(L_{0.5}A_{0.5})_{0.06}ZO$ thin film fluctuate by 3.7% and

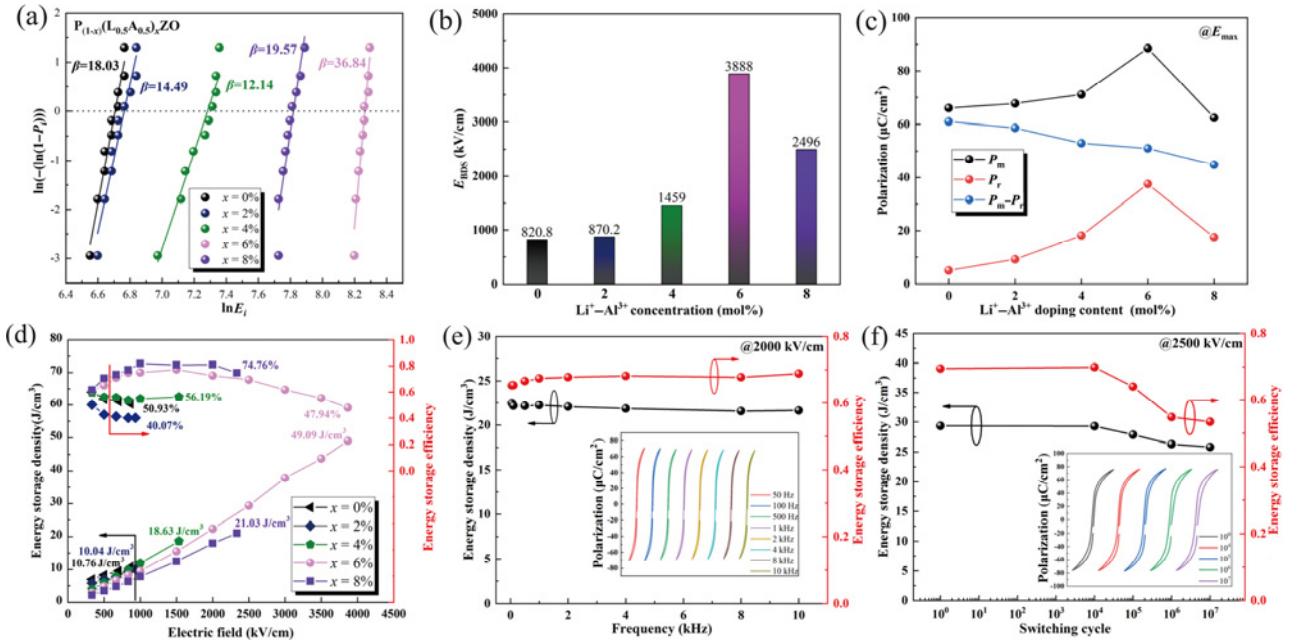

Fig. 6 (a) Weibull distributions, (b) E_{BDS} values, and (c) P_m, P_r, and $P_m - P_r$ values of $P_{(1-x)}(L_{0.5}A_{0.5})_xZO$ thin films with different Li^+–Al^{3+} doping contents. (d) Energy storage performances of $P_{(1-x)}(L_{0.5}A_{0.5})_xZO$ thin films at different E. (e) Frequency and (f) fatigue stability of energy storage performance; the insets show the corresponding P–E loops.

3.5%, respectively, exhibiting the superior frequency stability. Besides, in the practical application, the working E of film capacitors is far below the E_{BDS} value. Herein, a triangular wave with a magnitude of 2500 kV/cm is applied to fatigue endurance testing. As shown in Fig. 6(f), the W_{rec} and η degrade after 10^5 cycles, which are decreased by 12.1% and 16.1% after 10^7 cycles, respectively, due to the polarization fatigue effect.

According to the above-mentioned results, doping ions deeply influence the polariazation behaviors of PZO films. Although the discharge energy density has been significantly improved, the large P_r, due to the relaxor FE-like characterization, is not conducive to achieving high efficiency in $P_{0.94}(L_{0.5}A_{0.5})_{0.06}ZO$ thin film. Accordingly, low-temperature annealing is employed to regulate the crystallization, suppress P loss, and increase the η. The crystal structure characterizations of the $P_{0.94}(L_{0.5}A_{0.5})_{0.06}ZO$ thin films at different annealing temperatures (500, 550, 600, 650, and 700 ℃) have been conducted by the XRD patterns, as shown in Fig. 7(a), which exhibit a pure polycrystalline perovskite structure without detectable secondary phases for the films annealed at 650 and 700 ℃. In contrast, the diffraction peaks corresponding to the perovskite phase disappear for the films annealed below 600 ℃, while a broad diffraction peak appears around 29° due to the formation of the pyrochlore phase, representing the amorphous structure [44–46]. Figures 7(b1)–7(b5) show the cross-sectional SEM images of the $P_{0.94}(L_{0.5}A_{0.5})_{0.06}ZO$ thin films at different annealing temperatures. The films' thickness is about 300 nm, and no obvious structural defects such as void or crack can be observed. In order to further confirm the changed crystallization degree induced by regulating the annealing temperature, the surface morphologies are characterized by using the AFM, as shown in Figs. 7(c1)–7(c5). It can be seen that the films' surface is smooth, and no visible grains appear in the $P_{0.94}(L_{0.5}A_{0.5})_{0.06}ZO$ thin film annealed at 500 ℃; conversely, the fine grains can be seen in the films annealed above 650 ℃, accompanying an increase in the root mean square (RMS) values from 0.97 to 4.31 nm as the annealing temperature increases. These findings further verify that the phase composition and microstructure of the $P_{0.94}(L_{0.5}A_{0.5})_{0.06}ZO$ thin films can be controlled by the annealing temperature.

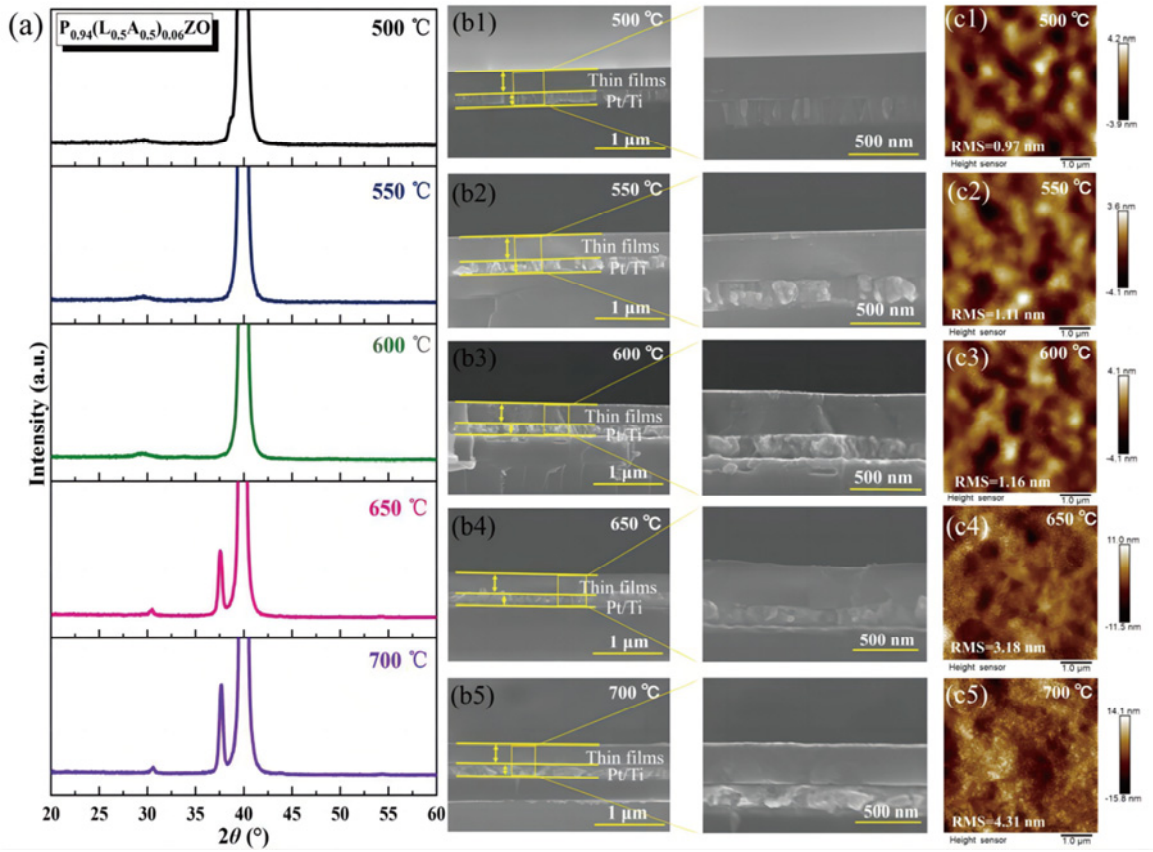

Fig. 7 (a) XRD patterns, (b1–b5) cross-sectional SEM images, and (c1–c5) AFM surface morphology images of the thin films at different annealing temperatures.

Figure 8(a) and Figs. S4(a)–S4(d) in the ESM show the *P*–*E* loops of $P_{0.94}(L_{0.5}A_{0.5})_{0.06}ZO$ thin films annealed at different temperatures. The shape of the *P*–*E* loop for the films annealed below 600 ℃ shows a linear-like polarization characteristic, accompanying both lower P_m and P_r values due to the amorphous or semi-crystalline structure. Once the annealing temperature is above 650 ℃, the *P*–*E* loops show the relaxor FE-like polarization characteristic as well as the significant increases in both P_m and P_r (85.71 μC/cm^2 and 24.79 μC/cm^2 for the film annealed at 700 ℃, respectively), ascribing to the enhanced crystallization degree for $P_{0.94}(L_{0.5}A_{0.5})_{0.06}ZO$ thin films. The comparison diagram of the monopolar *P*–*E* loops at E_{max} is shown in Fig. 8(b). It can be seen that the P_m values increase gradually with the increasing annealing temperature due to better crystallization; in contrast, the bearable E_{max} is much higher in the films with low annealing temperatures due to that there is less grain and domain boundary conduction. As shown in Fig. 8(c), the $P_m - P_r$ values are 21.03, 26.22, 26.35, 44.24, and 51.02 μC/cm^2 as the annealing temperature increases. Figure 8(d) and Fig. S4(e) in the ESM show the E_{BDS} values of $P_{0.94}(L_{0.5}A_{0.5})_{0.06}ZO$ films annealed at different temperatures. As the annealing temperature increases, the maximum E_{BDS} value is obtained at 550 ℃, attributing to the pyrochlore phase acted as charge trap center and smooth surface morphology [44,47–49], where much more valley morphologies can be seen in the films annealed at 500 ℃ compared to those at 550 ℃, meaning that the excessively lower annealing temperature may induce more voids or structural defects [47]. Specifically, the moderate *P*, good electric field endurance, and the slimmer *P*–*E* loops in $P_{0.94}(L_{0.5}A_{0.5})_{0.06}ZO$ thin film annealed at 550 ℃ are favorable to generate excellent energy storage performance.

The W_{rec} and η of $P_{0.94}(L_{0.5}A_{0.5})_{0.06}ZO$ thin films annealed at different temperatures are shown in Fig. 9(a) and Fig. S5 in the ESM, and it can be seen that the W_{rec} gradually increases with the increase of *E*. The films annealed at 650 and 700 ℃ possess much higher W_{rec} under the same *E* comparing to those annealed below 600 ℃, caused by the good crystallization and large $P_m - P_r$ values. However, the η is lower than 50% for the films annealed at 650 and 700 ℃ due to the high P_r and serious W_{loss} [50]. Instead, $P_{0.94}(L_{0.5}A_{0.5})_{0.06}ZO$ thin films annealed below 600 ℃ display linear-like polarization behavior rather than FE-like behavior, and

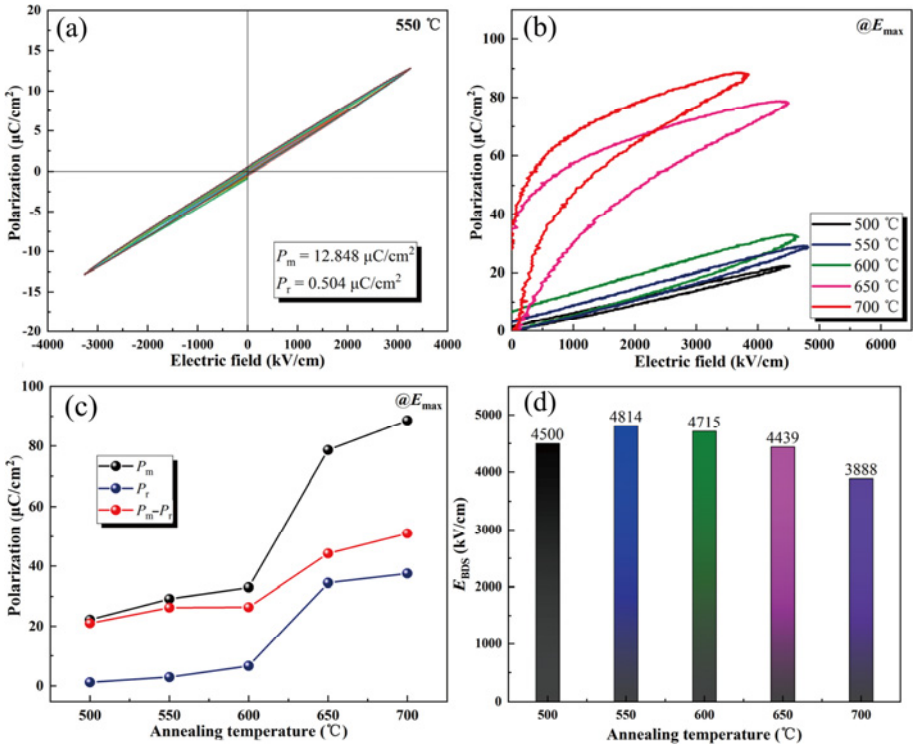

Fig. 8 (a) *P*–*E* loops of $P_{0.94}(L_{0.5}A_{0.5})_{0.06}ZO$ thin films annealed at 550 ℃. (b) Monopolar *P*–*E* loops of $P_{0.94}(L_{0.5}A_{0.5})_{0.06}ZO$ thin films annealed at different temperatures. (c) P_m, P_r, and $P_m - P_r$ values measured at E_{max}. (d) E_{BDS} of $P_{0.94}(L_{0.5}A_{0.5})_{0.06}ZO$ thin films at different annealing temperatures.

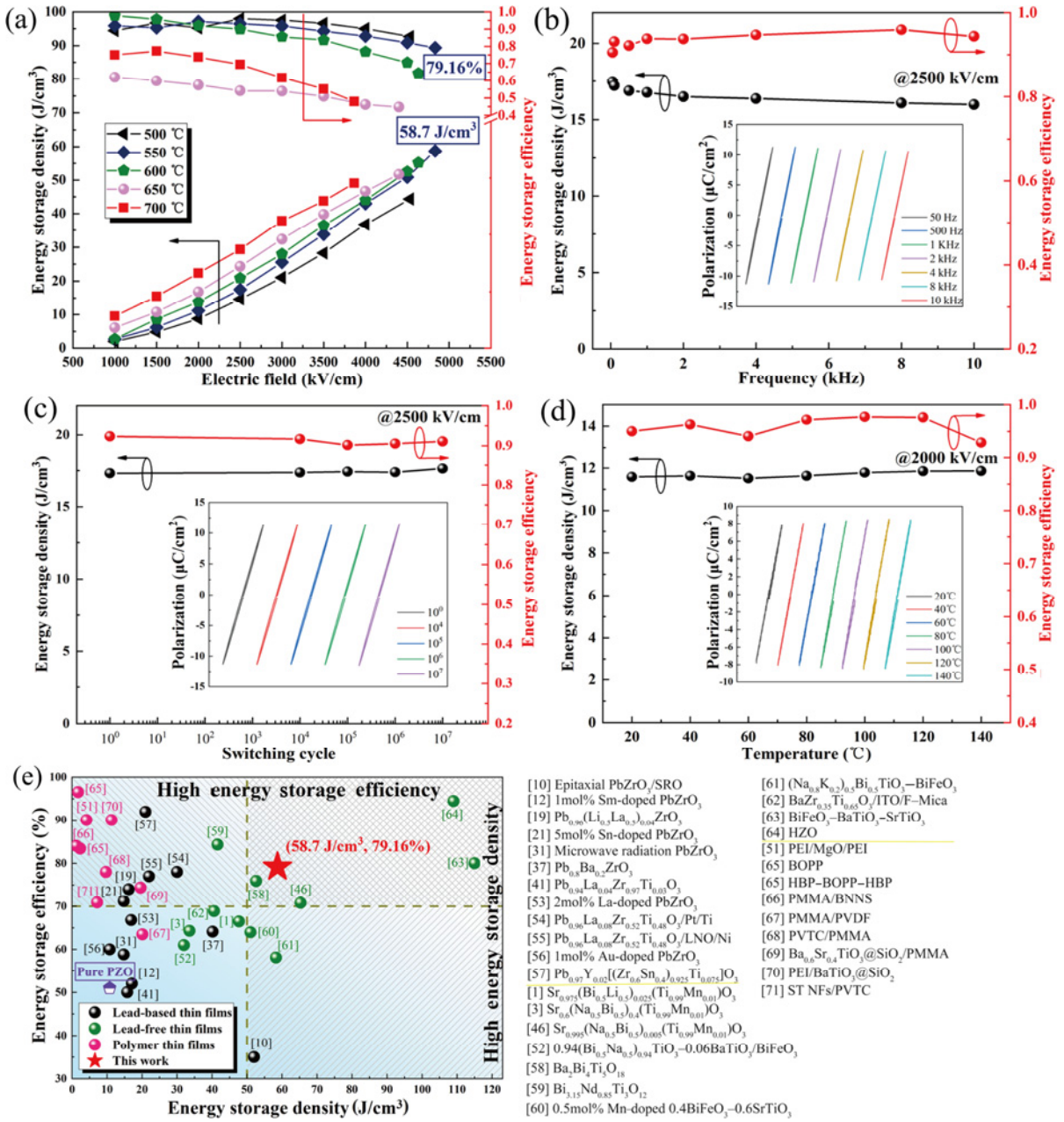

Fig. 9 Energy storage performances of $P_{0.94}(L_{0.5}A_{0.5})_{0.06}ZO$ thin films of different annealing temperatures as functions of (a) E, (b) frequency, (c) fatigue cycle, and (d) temperature. The insets show the corresponding P–E loops. (e) Comparisons of energy storage performances of $P_{0.94}(L_{0.5}A_{0.5})_{0.06}ZO$ films, representative polymer films, and lead-containing and lead-free inorganic films [1,3,10,12,19,21,31,37,41,46,51–71].

the ultra-low P_r as well as good electric field endurance endurance is obtained in the $P_{0.94}(L_{0.5}A_{0.5})_{0.06}ZO$ thin film annealed at 550 ℃, possessing the superior W_{rec} of 58.7 J/cm^3 and η of 79.16%, exhibiting excellent frequency, cyclic fatigue, and temperature stability, as shown in Figs. 9(b)–9(d). The comparison of this work with the representative polymer films and lead-containing and lead-free inorganic films are summarized (Fig. 9(e)). Although polymer films always possess high E_{BDS}, the low ε_r makes the low W_{rec} (e.g., the η of polyetherimide (PEI)/MgO/PEI is above 90%, while the W_{rec} is only 4.13 J/cm^3) [51]. The inorganic films usually exhibit high P but suffer low endurable E, resulting in the high W_{rec} and low η (e.g., the W_{rec} of $0.94(Bi_{0.5}Na_{0.5})_{0.94}TiO_3$–$0.06BaTiO_3$/$BiFeO_3$ is 31.96 J/cm^3, but η is only 61%) [52]. In comparison, the superior energy storage performances are achieved in the resultant $P_{0.94}(L_{0.5}A_{0.5})_{0.06}ZO$ thin film annealed at 550 ℃.

4 Conclusions

In summary, an efficient way to improve the energy storage performances of PZO thin films has been proposed, and combining the ionic pair doping with low-temperature annealing can effectively regulate the polariazation behaviors of PZO films. The FE-like *P* instead of the *E*-induced double *P*–*E* loop characteristic is obtained when the doping content of Li^{+}–Al^{3+} ionic pair reaches 6%. Furthermore, a linear-like polarization characteristic is also achieved by lowering the annealing temperature. The low P_r as well as high E_{BDS} enables the $P_{0.94}(L_{0.5}A_{0.5})_{0.06}ZO$ thin film annealed at 550 ℃ to have the superior W_{rec} of 58.7 J/cm^3 and efficiency of 79.16%, accompanying the excellent frequency, high temperature stability, and good electric fatigue tolerance.

Acknowledgements

This work was supported by the National Natural Science Foundation of China (Nos. 52277024, U20A20308, and 51977050), Heilongjiang Provincial Natural Science Foundation of China (No. ZD2020E009), China Postdoctoral Science Foundation (Nos. 2021T140166 and 2018M640303), Heilongjiang Province Postdoctoral Science Foundation (No. LBH-Z18099), and University Nursing Program for Young Scholars with Creative Talents in Heilongjiang (No. UNPYSCT-2020178). Tiandong Zhang acknowledges the supports from China Scholarship Council (CSC) and China Association for Science and Technology.

Declaration of competing interest

The authors have no competing interests to declare that are relevant to the content of this article.

Electronic Supplementary Material

Supplementary material is available in the online version of this article at https://doi.org/10.26599/JAC.2023.9220728.

References

[1] Yang XR, Li WL, Zhang YL, *et al*. High energy storage density achieved in Bi^{3+}–Li^{+} co-doped $SrTi_{0.99}Mn_{0.01}O_3$ thin film via ionic pair doping-engineering. *J Eur Ceram Soc* 2020, **40**: 706–711.

[2] Liu XJ, Zheng MS, Chen G, *et al*. High-temperature polyimide dielectric materials for energy storage: Theory, design, preparation and properties. *Energy Environ Sci* 2022, **15**: 56–81.

[3] Zhang YL, Li WL, Qiao YL, *et al*. 0.6ST–0.4NBT thin film with low level Mn doping as a lead-free ferroelectric capacitor with high energy storage performance. *Appl Phys Lett* 2018, **112**: 093902.

[4] Feng Y, Xue JP, Zhang TD, *et al*. Double-gradients design of polymer nanocomposites with high energy density. *Energy Storage Mater* 2022, **44**: 73–81.

[5] Feng Y, Tang WX, Zhang Y, *et al*. Machine learning and microstructure design of polymer nanocomposites for energy storage application. *High Volt* 2022, **7**: 242–250.

[6] Shao YL, El-Kady MF, Sun JY, *et al*. Design and mechanisms of asymmetric supercapacitors. *Chem Rev* 2018, **118**: 9233–9280.

[7] Wang G, Lu ZL, Li Y, *et al*. Electroceramics for high-energy density capacitors: Current status and future perspectives. *Chem Rev* 2021, **121**: 6124–6172.

[8] Winter M, Brodd RJ. What are batteries, fuel cells, and supercapacitors? *Chem Rev* 2004, **104**: 4245–4270.

[9] Sazali N, Wan Salleh WN, Jamaludin AS, *et al*. New perspectives on fuel cell technology: A brief review. *Membranes* 2020, **10**: 99.

[10] Ko DL, Hsin T, Lai YH, *et al*. High-stability transparent flexible energy storage based on $PbZrO_3$/muscovite heterostructure. *Nano Energy* 2021, **87**: 106149.

[11] Sun ZX, Wang Z, Tian Y, *et al*. Progress, outlook, and challenges in lead-free energy-storage ferroelectrics. *Adv Electron Mater* 2020, **6**: 1900698.

[12] Thatikonda SK, Huang WH, Du XR, *et al*. Sm-doping induced large enhancement of antiferroelectric and energy storage performances of (111) oriented $PbZrO_3$ thin films. *Ceram Int* 2019, **45**: 23586–23591.

[13] Li YZ, Wang ZJ, Bai Y, *et al*. High energy storage performance in Ca-doped $PbZrO_3$ antiferroelectric films. *J Eur Ceram Soc* 2020, **40**: 1285–1292.

[14] Qiao LL, Song C, Sun YM, *et al*. Observation of negative capacitance in antiferroelectric $PbZrO_3$ films. *Nat Commun* 2021, **12**: 4215.

[15] Hao XH, Zhai JW, Zhou J, *et al*. Structure and electrical properties of $PbZrO_3$ antiferroelectric thin films doped with barium and strontium. *J Alloys Compd* 2011, **509**: 271–275.

[16] Hao XH, Zhai JW, Yao X. Improved energy storage performance and fatigue endurance of Sr-doped $PbZrO_3$ antiferroelectric thin films. *J Am Ceram Soc* 2009, **92**: 1133–1135.

[17] Parui J, Krupanidhi SB. Enhancement of charge and energy storage in sol–gel derived pure and La-modified $PbZrO_3$ thin films. *Appl Phys Lett* 2008, **92**: 192901.

[18] Ye M, Li T, Sun Q, *et al*. A giant negative electrocaloric effect in Eu-doped $PbZrO_3$ thin films. *J Mater Chem C* 2016, **4**: 3375–3378.

[19] Zhang TD, Zhao Y, Li WL, *et al*. High energy storage

density at low electric field of ABO_3 antiferroelectric films with ionic pair doping. *Energy Storage Mater* 2019, **18**: 238–245.

[20] Zhang J, Zhang YY, Chen QQ, *et al*. Enhancement of energy-storage density in PZT/PZO-based multilayer ferroelectric thin films. *Nanomaterials* 2021, **11**: 2141.

[21] Guo X, Ge J, Ponchel F, *et al*. Effect of Sn substitution on the energy storage properties of high (001)-oriented $PbZrO_3$ thin films. *Thin Solid Films* 2017, **632**: 93–96.

[22] Ye M, Sun Q, Chen XQ, *et al*. Effect of Nb doping on preferential orientation, phase transformation behavior and electrical properties of $PbZrO_3$ thin films. *J Alloys Compd* 2012, **541**: 99–103.

[23] Carabatos-Nedelec C, El Harrad I, Handerek J, *et al*. Structural and spectroscopic studies of niobium doped PZT 95/5 ceramics. *Ferroelectrics* 1992, **125**: 483–488.

[24] Cordero F, Buixaderas E, Galassi C. Damage from coexistence of ferroelectric and antiferroelectric domains and clustering of O vacancies in PZT: An elastic and Raman study. *Materials* 2019, **12**: 957.

[25] Sa TL, Qin N, Yang GW, *et al*. W-doping induced antiferroelectric to ferroelectric phase transition in $PbZrO_3$ thin films prepared by chemical solution deposition. *Appl Phys Lett* 2013, **102**: 172906.

[26] Dobal PS, Katiyar RS, Bharadwaja SSN, *et al*. Micro-Raman and dielectric phase transition studies in antiferroelectric $PbZrO_3$ thin films. *Appl Phys Lett* 2001, **78**: 1730–1732.

[27] Shangguan DD, Duan YN, Wang BL, *et al*. Enhanced energy-storage performances of $(1-x)PbZrO_3$–$xPbSnO_3$ antiferroelectric thin films under low electric fields. *J Alloys Compd* 2021, **870**: 159440.

[28] Lin ZJ, Chen Y, Liu Z, *et al*. Large energy storage density, low energy loss and highly stable $(Pb_{0.97}La_{0.02})(Zr_{0.66}Sn_{0.23}Ti_{0.11})O_3$ antiferroelectric thin-film capacitors. *J Eur Ceram Soc* 2018, **38**: 3177–3181.

[29] Gao R, Reyes-Lillo SE, Xu RJ, *et al*. Ferroelectricity in $Pb_{1+\delta}ZrO_3$ thin films. *Chem Mater* 2017, **29**: 6544–6551.

[30] Hao XH, Zhai JW, Kong LB, *et al*. A comprehensive review on the progress of lead zirconate-based antiferroelectric materials. *Prog Mater Sci* 2014, **63**: 1–57.

[31] Fang Y, Bai Y, Li YZ, *et al*. Improved energy storage performance of $PbZrO_3$ antiferroelectric thin films crystallized by microwave radiation. *RSC Adv* 2021, **11**: 18387–18394.

[32] Qi H, Zuo RZ. Linear-like lead-free relaxor antiferroelectric $(Bi_{0.5}Na_{0.5})TiO_3$–$NaNbO_3$ with giant energy-storage density/efficiency and super stability against temperature and frequency. *J Mater Chem A* 2019, **7**: 3971–3978.

[33] Qi H, Zuo RZ, Xie AW, *et al*. Ultrahigh energy-storage density in $NaNbO_3$-based lead-free relaxor antiferroelectric ceramics with nanoscale domains. *Adv Funct Mater* 2019, **29**: 1903877.

[34] Yang CH, Qian J, Han YJ, *et al*. Design of an all-inorganic flexible $Na_{0.5}Bi_{0.5}TiO_3$-based film capacitor with giant and stable energy storage performance. *J Mater Chem A* 2019, **7**: 22366–22376.

[35] Ke SM, Fan HQ, Huang HT, *et al*. Lorentz-type relationship of the temperature dependent dielectric permittivity in ferroelectrics with diffuse phase transition. *Appl Phys Lett* 2008, **93**: 112906.

[36] Shvartsman VV, Zhai J, Kleemann W. The dielectric relaxation in solid solutions $BaTi_{1-x}Zr_xO_3$. *Ferroelectrics* 2009, **379**: 77–85.

[37] Peng BL, Zhang Q, Li X, *et al*. Large energy storage density and high thermal stability in a highly textured (111)-oriented $Pb_{0.8}Ba_{0.2}ZrO_3$ relaxor thin film with the coexistence of antiferroelectric and ferroelectric phases. *ACS Appl Mater Interfaces* 2015, **7**: 13512–13517.

[38] Wei XY, Feng YJ, Yao X. Dielectric relaxation behavior in barium stannate titanate ferroelectric ceramics with diffused phase transition. *Appl Phys Lett* 2003, **83**: 2031–2033.

[39] Jeon SC, Kang SJL. Coherency strain enhanced dielectric–temperature property of rare-earth doped $BaTiO_3$. *Appl Phys Lett* 2013, **102**: 112915.

[40] Shvartsman VV, Lupascu DC. Lead-free relaxor ferroelectrics. *J Am Ceram Soc* 2012, **95**: 1–26.

[41] Zhang Y, Li Y, Hao XH, *et al*. Flexible antiferroelectric thick film deposited on nickel foils for high energy-storage capacitor. *J Am Ceram Soc* 2019, **102**: 6107–6114.

[42] Yang CH, Lv PP, Qian J, *et al*. Fatigue-free and bending-endurable flexible Mn-doped $Na_{0.5}Bi_{0.5}TiO_3$–$BaTiO_3$–$BiFeO_3$ film capacitor with an ultrahigh energy storage performance. *Adv Energy Mater* 2019, **9**: 1803949.

[43] Zou D, Liu SY, Zhang C, *et al*. Flexible and translucent PZT films enhanced by the compositionally graded heterostructure for human body monitoring. *Nano Energy* 2021, **85**: 105984.

[44] Li YZ, Lin JL, Bai Y, *et al*. Ultrahigh-energy storage properties of $(PbCa)ZrO_3$ antiferroelectric thin films via constructing a pyrochlore nanocrystalline structure. *ACS Nano* 2020, **14**: 6857–6865.

[45] Rabuffetti FA, Brutchey RL. Tailoring the mechanism of the amorphous-to-crystalline phase transition of $PbTiO_3$ via kinetically controlled hydrolysis. *Chem Mater* 2011, **23**: 4063–4076.

[46] Chen YN, Wang ZJ, Yang T, *et al*. Crystallization kinetics of amorphous lead zirconate titanate thin films in a microwave magnetic field. *Acta Mater* 2014, **71**: 1–10.

[47] Zhang TD, Li WL, Zhao Y, *et al*. High energy storage performance of opposite double-heterojunction ferroelectricity-insulators. *Adv Funct Mater* 2018, **28**: 1706211.

[48] Zhang TD, Yin C, Zhang CH, *et al*. Self-polarization and energy storage performance in antiferroelectric-insulator multilayer thin films. *Compos Part B* 2021, **221**: 109027.

[49] Zhang YL, Li WL, Wang ZY, *et al*. Ultrahigh energy storage and electrocaloric performance achieved in $SrTiO_3$ amorphous thin films via polar cluster engineering. *J Mater Chem A* 2019, **7**: 17797–17805.

[50] Liang ZS, Liu M, Ma CR, *et al*. High-performance

$BaZr_{0.35}Ti_{0.65}O_3$ thin film capacitors with ultrahigh energy storage density and excellent thermal stability. *J Mater Chem A* 2018, **6**: 12291–12297.

[51] Zhang TD, Yang LY, Zhang CH, *et al*. Polymer dielectric films exhibiting superior high-temperature capacitive performance by utilizing an inorganic insulation interlayer. *Mater Horiz* 2022, **9**: 1273–1282.

[52] Chen P, Wu SH, Li P, *et al*. Great enhancement of energy storage density and power density in BNBT/*x*BFO multilayer thin film hetero-structures. *Inorg Chem Front* 2018, **5**: 2300–2305.

[53] Koo CY, Eum YJ, Hwang SO, *et al*. Development of high energy capacitors using La-doped $PbZrO_3$ anti-ferroelectric thin films. *Ferroelectrics* 2014, **465**: 89–95.

[54] Hu ZQ, Ma BH, Liu SS, *et al*. Relaxor behavior and energy storage performance of ferroelectric PLZT thin films with different Zr/Ti ratios. *Ceram Int* 2014, **40**: 557–562.

[55] Tong S, Ma BH, Narayanan M, *et al*. Lead lanthanum zirconate titanate ceramic thin films for energy storage. *ACS Appl Mater Interfaces* 2013, **5**: 1474–1480.

[56] Li YZ, Wang ZJ, Bai Y, *et al*. Enhancement of energy storage density in antiferroelectric $PbZrO_3$ films via the incorporation of gold nanoparticles. *J Am Ceram Soc* 2019, **102**: 5253–5261.

[57] Ahn CW, Amarsanaa G, Won SS, *et al*. Antiferroelectric thin-film capacitors with high energy-storage densities, low energy losses, and fast discharge times. *ACS Appl Mater Interfaces* 2015, **7**: 26381–26386.

[58] Yang BB, Guo MY, Li CH, *et al*. Flexible ultrahigh energy storage density in lead-free heterostructure thin-film capacitors. *Appl Phys Lett* 2019, **115**: 243901.

[59] Song DP, Yang J, Sun JX, *et al*. Controlling the crystallization of Nd-doped $Bi_4Ti_3O_{12}$ thin-films for lead-free energy storage capacitors. *J Appl Phys* 2020, **127**: 224102.

[60] Pan H, Zeng Y, Shen Y, *et al*. $BiFeO_3$–$SrTiO_3$ thin film as a new lead-free relaxor-ferroelectric capacitor with ultrahigh energy storage performance. *J Mater Chem A* 2017, **5**: 5920–5926.

[61] Han YJ, Qian J, Yang CH. Time-stable giant energy density and high efficiency in lead free (Ce,Mn)-modified $(Na_{0.8}K_{0.2})_{0.5}Bi_{0.5}TiO_3$ ceramic film capacitor. *Ceram Int* 2019, **45**: 22737–22743.

[62] Liang ZS, Liu M, Shen LK, *et al*. All-inorganic flexible embedded thin-film capacitors for dielectric energy storage with high performance. *ACS Appl Mater Interfaces* 2019, **11**: 5247–5255.

[63] Pan H, Li F, Liu Y, *et al*. Ultrahigh-energy density lead-free dielectric films via polymorphic nanodomain design. *Science* 2019, **365**: 578–582.

[64] Hoffmann M, Fengler FPG, Max B, *et al*. Negative capacitance for electrostatic supercapacitors. *Adv Energy Mater* 2019, **9**: 1901154.

[65] Han CC, Zhang XH, Chen D, *et al*. Enhanced dielectric properties of sandwich-structured biaxially oriented polypropylene by grafting hyper-branched aromatic polyamide as surface layers. *J Appl Polym Sci* 2020, **137**: 48990.

[66] Liu FH, Li Q, Li ZY, *et al*. Poly(methyl methacrylate)/boron nitride nanocomposites with enhanced energy density as high temperature dielectrics. *Compos Sci Technol* 2017, **142**: 139–144.

[67] Chi QG, Zhou YH, Yin C, *et al*. A blended binary composite of poly(vinylidene fluoride) and poly(methyl methacrylate) exhibiting excellent energy storage performances. *J Mater Chem C* 2019, **7**: 14148–14158.

[68] Feng MJ, Zhang TD, Song CH, *et al*. Improved energy storage performance of all-organic composite dielectric via constructing sandwich structure. *Polymers* 2020, **12**: 1972.

[69] Zhang TD, Zhao XW, Zhang CH, *et al*. Polymer nanocomposites with excellent energy storage performances by utilizing the dielectric properties of inorganic fillers. *Chem Eng J* 2020, **408**: 127314.

[70] Feng Y, Zhou YH, Zhang TD, *et al*. Ultrahigh discharge efficiency and excellent energy density in oriented core–shell nanofiber-polyetherimide composites. *Energy Storage Mater* 2020, **25**: 180–192.

[71] Xue JP, Zhang TD, Zhang CH, *et al*. Excellent energy storage performance for P(VDF–TrFE–CFE) composites by filling core–shell structured inorganic fibers. *J Mater Sci Mater Electron* 2020, **31**: 21128–21141.